Design of a Multi-Mode Power Management System for Electric Vehicles with Grid Integration

Tayyaba Gul Tareen*, Muhammad Aamir **, Jehanzeb Khan*, Ghassan Husnain *, Fakhar Anjam ******

* Department of Electrical Engineering, IQRA National University, Peshawar 25100, Pakistan;
** Department of Electrical and Computer Engineering, Pak Austria Fachhochschule, Institute of Applied Science and Technology, Haripur, Pakistan;
*** Department of Computer Science, CECOS University of IT & Emerging Sciences, Peshawar, Pakistan.
**** Department of Electrical Engineering, University of Science & Technology Bannu, Pakistan.

Abstract- Vehicle-to-Grid (V2G) and Grid-to-Vehicle (G2V) are innovative concepts that leverage the bidirectional flow of energy between electric vehicles and the electrical grid, allowing to consume energy and contribute surplus energy back to the grid when parked (at resting state). This dynamic interaction can help in balancing electricity demand and supply, enhance the grid stability, and optimize the integration of renewable energy sources. The advancement in electric vehicle battery and charger technologies has enhanced the overall electric vehicle capabilities, promoting broader adoption. While electric vehicles offer environmental and economic advantages, the charging process can exert adverse effects on existing network operations. To address these issues, suitable charging management strategies are still in the research process. Therefore, a battery charging infrastructure with multiple features using minimum number of semiconductor components is the need and demand of time. However, many solutions of V2G and G2V use greater number of switches. Which increase the weight and size of the charging infrastructure as the most challenging task. In this research, a novel V2G and G2V infrastructure with minimum number of switches and Active Power Filter, working in three modes of operation has been proposed. In V2G mode, the inverter/rectifier part of the charging system can feed the available power at the dc link into the grid. In addition, in G2Vmode, it can generate the power into the dc-link for onward submission into the battery bank. In this study the proposed system consists of a back-end novel high current density bidirectional converter connected with the battery bank of the vehicle and a three-phase inverter/rectifier at the front, connected with the grid. The high current density current is specially designed to manage high input current from the battery with minimum number of the switches. Moreover, high frequency transformer is employed as a galvanic isolation to isolate the grid from the battery bank. The proposed converter can successfully step-up the low battery bank voltage to high dc-link voltage in order, to feed its battery bank power into the grid according to the system need. On the other hand, in reverse mode of operation, the dc-link voltage can be step down from dc-link voltage to low battery bank voltage. This paper provides an intricate control scheme i.e. model predictive control (MPC) designed for the high current density bidirectional dc-dc converter and the inverter/rectifier. The MPC ensures a promising regulating operation of a bidirectional dc-dc converter by providing constant voltage at the dc-link and regulate the power sharing into the grid at the inverter. In active power filter mode, when the system remains idle and there is no vehicle connected to the grid, the system works as active power filter and remove the harmonics inside the grid which may be generated by different non-liner loads connected in the same grid. The intensive simulation using MATLAB/Simulink validate the performance of the circuit as well as the control schemes for all the subparts of the proposed system. The switches stress and the output/input voltages of the high current density bidirectional dc-dc converter shows superior performance with minimum number of switches. The results verify that, the MPC control of inverter shows superior performance with THD of 0.68% for linear load. The feasibility of the suggested topology and its outstanding performance in addressing both V2G and G2V mode of operation have been confirmed through simulation outcomes. It effectively compensates reactive power and mitigates current harmonic distortion selectively.

Index Terms- Bidirectional converter, Model Predictive control, vehicle to grid, grid to vehicle, grid system

I. Introduction

This In recent years, due to high carbon dioxide CO_2 emission into the atmosphere causes high environmental issues in the world. Likewise, high penetration, uncontrolled charging and extreme power load demand of the conventional automobile has been raised into the distribution grid [1]. These practical issues damage the reliability, sustainability, and high harmonic penetration of the power distribution grid [2]. These problems have forced humans to think about the development of smart sustainable vehicles in the field of transportation, energy, cost, battery size and complete management issues. Furthermore, it significantly reduces CO_2 emissions from road traffic [3]. In two major renewable energy systems, RES systems i.e. photovoltaic PV and wind energy WE, utilizes numerous inverters in the system as the main device for the change of DC power to AC power. In power systems connected with the grid, the output sinusoidal waveform is scaled between the range of low-power kilowatt to the higher-power megawatt.

Therefore, inverters fulfills its part in the development of wind generation and large-scale PV systems making the subject inverters more essential [4].

Recently, many electric vehicle EV systems are used as smart loads to provide a power line and conditioning of voltage into the distribution grid. Wind energy systems and integrated grid-PV installation causes the issue of complex PQ, heat, and harmonics into the power grid. Hence, affecting the voltage sinusoidal waveform spectra and the current supply [5], with regard to poor system efficiency, faulty performance of machines and electric cables, overheating of transformers, power failure, prerequisite of power safety devices [6, 7]. The resources of energy are erratic, and the renewable power system produces conditional output. Hence, several PQ mitigations and defined current harmonics techniques are needed for improving the overall performance of distribution grid system. Nowadays, electricity is the most demanding commodity from tiny household utilities to high level commercial industries. To reduce stress on the national power grid two major RES, like solar photovoltaic (PV) and wind energy (WE) system installed with electricity distribution infrastructure. With the use of the storage devices and distributed energy resources (DER) not only the distribution grid but the reliability and power quality (PQ) is also improved. In addition, this RES system minimizes the power loss for AC transmission and distribution networks. The adoption of EVs has become an achievable approach to lessen the negative environmental effects of conventional engine combustion in completely traditional automobiles. The worry that one would run out of battery power before arriving at a charging station is one of the major concerns among potential EVs consumers. Another main concern is the infrastructure for charging EVs, which is not as widespread and developed as the network of gasoline stations. Innovations in battery charger technology are also essential for lowering expenses, boosting power density, and resolving green issues to maximum level. The extensive use of EVs may put stress on the existing electrical grids, particularly during peak periods of charging EVs batteries demand is the highest [8]. EVs battery chargers work in dual mode of operation i.e. G2V and V2G with a cascade connection of DC-DC converters and AC-DC converters [9]. By using dual active bridge (DAB) converter as the bidirectional DC-DC converter works well in both the scenarios but due to its challenging nature at high switching frequencies the need of more advance flyback-back converter is the ultimate requirement and a need of MPC control technique which not only reduce system cost but also upgrade performance of the system by minimizing the amount of switches to a good level and improve system efficiency to a satisfactory level [10]. In EV battery systems connected to the grid, the performance is impacted by various current and voltage harmonics. Additionally, nonlinear loads, and the integration of RES significantly affect the power networks efficiency and overall performance of the system PQ. These issues could be address by taking help from the APFs [11]. This study purposes to reduce the number of switching devices to reduce the overall cost, dimensions, and mass of the inverters connected with the power grid [12].

The smart and coordinated charging of the EVs makes them the most popular utilities in the recent world. Therefore, the EV high-tech advancements are gaining popularity day by day. In this domain of research and technological development, the smart EVs, power train, smart battery charger and coordinated charging infrastructure has been the focus of the modern equipment expansion. The universal battery charger circuit connected with the power grid is illustrated in Figure 1. The AC current from the power grid is used to charge the EV battery. Several EV batteries charging configurations are available in the market, (a) Universal battery charging system (b) Grid-connected PV-EV battery charging system (c) Stand-alone PV-EV battery charging system and (d) Grid-connected WTG-EV battery charging system [13]. Other resources like RE can be utilized to power the EV battery, according to rating and functions. PV and Wind power stand to be the greatest standalone RES and grid connected solutions at different levels for charging the EV batteries [14].

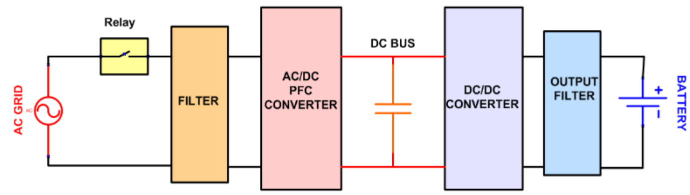

Figure 1. Universal battery charger

The EVs battery chargers are categorized into two main types such as on-board and off-board chargers. The on-board charger operates at low power rating and is installed inside the vehicle. However, the off-board chargers operate at powerful category and are installed on the ground. The on-board chargers have limitations like space, volumetric size, cost and charging time [15]. To solve this issue, the EV motor drives are operated as filter inductors or isolated transformers with the battery charger [16-19]. The on-board charger can operate as an inductive system or conductive system. The static charger utilizes a secondary winding inductor in the EV and main winding inductor in the charging station. This system is identified as a stationary inductive charger. To transfer the high rated power, a main paddle port is installed to the EV and the power is transfer in the magnetically operation. The inductive system transfers energy magnetically in the static or dynamic manner in the level 1 and level 2 rating system [11, 20, 21]. However, the conductive system transfer energy directly connecting the charger plug and EV [22]. The Dynamic charger operates in the wireless or contactless EV charging, when the EV is moving on the road. The energy is directed in both directions (unidirectional or bidirectional), between the fixed primary inductor and the EV charging.

During the unidirectional energy flow system, the energy is transmitted from G2V. Although, popular two-way energy flow charger, the power is transmitted in between the V2G and vice versa [23, 24]. The G2V charging system requires high power generation due to high energy transfer demand and uses additional alternative source with the power grid [25, 26]. The RES, for example wind and lunar energy exist the greatest favorable energy sources [27, 28]. These RES operate as an auxiliary source to charge the EV batteries without any CO_2 emissions of greenhouse gas emissions (GGE). The PV and wind energy sources are pollution free in nature and are limitless resources. The PV topped or wind generator are the best solutions for EV charging. The RES type EV power system operates at minimum electrical energy traffic throughout the highest hours [29-33]. Table 1. shows the SAE charging levels according to SAE EV conductive charge coupler standard (SAE J1772) [34]. Generally, the SAE charging rules are divided into three main levels such as level 1, level 2 and level 3 for both AC and DC battery charging. Level 1 is a slow charging method installed at the home or accessible power points. Similarly, level 2 is the partly fast charging method operated at the 240 V/400 V rating system. Level 3 is the three-phase fast charging method operated at 208 V/415 V charging system. Furthermore, for commercial and public usage a DC fast charging method is available [35-37]. The AC charging is adopted by the on-board charger installed inside the EV, while a DC charging is adopted by the off-board charger installed at fixed location on the ground [38, 39].

In recent times, different and wide range of solutions to the problems related to the quality of power has been suggested in electrical system. [41]. Different integrated filters are used with passive filters (PFs) in grid-integrated systems. It shows that with the use of upgraded filter technologies, power-quality problems can be resolved easily [42]. This could be static synchronous compensator, multilayered inverter, and APF and voltage regulator [43]. Generally, in the power industry linear and nonlinear loads are tested with renewable energy (RE) devices and are known as the nonlinear rectifier [44]. These solid states converters (loads) extract current harmonics and reactive power from the utility power. This extraction leads to altered waveforms in current and voltage signals, causing diverse interruptions, harmonic issues, and directly influencing human activities. To minimize system cost, weight, and size of the EV system operates with the transformers for isolation purpose with increased number of passive components. Yet topologies with no transformer meet reliable and improved system performance, minimum cost, compact size, and structure in comparison with old transformer-based topologies [45]. The demand for inverters is increasing every day, but they have a major drawback which is the increased number of switching components, transistors such as MOSFETs and IGBTs. Most of the SAPFs use components with high-power rating to enhance the power utilization factor in power plant and mitigation of current harmonic which makes its use limited. The higher the number of switching elements, generates increased losses in the switch when connected to the electrical grid and simultaneously generates increased number of harmonics in the output waveform, causing performance of the structure to deteriorate [46].

Now a day's reduced number of switches has become an upcoming conclusion in the field of power electronics EV and APF technology. Even with significant reduction in system components, there is a scarcity of literature and information on the reduced number of switches in electric vehicle-active power filters (EV-APFs). Hence, this paper will concentrate on designing a three-phase reduced switch count smart EV battery charger for grid-connected applications. In conclusion, the need for electric vehicles (EVs) and smart charging is needed to control the high peak energy demand and to protect the distribution grid. Therefore, intelligent devices and smart charging techniques are needed. Inspired by the above discussion, a transformer type smart EV battery charger is designed in coordination with the active power filters (APFs) capability. In addition, the improved design is tested with a minimum number of active components and passive components. Furthermore, it offers many advantages and works as a multifunctional EV battery system such as.

1) It reduces the price of the system, the weight, and the overall dimension size.

2) Provides superior and smart charging operation between different operating modes.

3) Enhanced reactive power support.

4) Harmonic functional mitigation capability.

II. SYSTEM DESCRIPTION

In this research, a novel bidirectional dc-dc converter with H-bridge topology for a three-phase EV battery charger is designed for reducing the system volumetric size and cost. The proposed circuit will operate as battery charger for EV. The circuit functions with multiple functional ability and operate as APF, smart and coordinated charging with high efficiency and reduced switch count configuration. The proposed system consists of two power circuits. The first circuit is the bidirectional converter which is extracted from the famous flyback converter as shown in Figure. 3. Since the current at the input of the circuit is very high, therefore the circuit is specially proposed to control high input current keeping intact the high efficiency of the circuit. Additionally, the circuit provides galvanic isolation, operating at high frequency with minimum number of switches and controlled using MPC. The second circuit consists of a conventional three phase converter which operates as an inverter during battery discharger and acts as a rectifier during battery charger. Moreover, the inverter also acts as an active power filter during full charge mode improving the quality of the power grid.

A. Modes of operation of proposed system:

1) Mode I: Charging mode (Rectifier mode)

In the charging mode (Figure 2), the converter will work as a rectifier and provides constant DC link voltage. The MPC controller will provide regulated DC link voltage while the dc-dc converter will charge the EV battery pack. This mode will operate until the EV is fully charged.

2) Mode II: Discharging mode (Rectifier mode)

In the discharging mode, the power in the EV battery pack can be utilized for the grid under the concept of Vehicle to Grid V2G where extra power from the battery can be injected back into the grid. During the discharging phase the DC-DC converter is used to provide regulated Dc-link voltage for inverter, whereas in the AC-DC stage, an inverter is used to control the grid current employing the model predictive control.

3) Mode III: APF mode

During the time when there is no vehicle connected to the system or the vehicle battery is fully charged with no V2G operation, the system will work as harmonic suppressor.

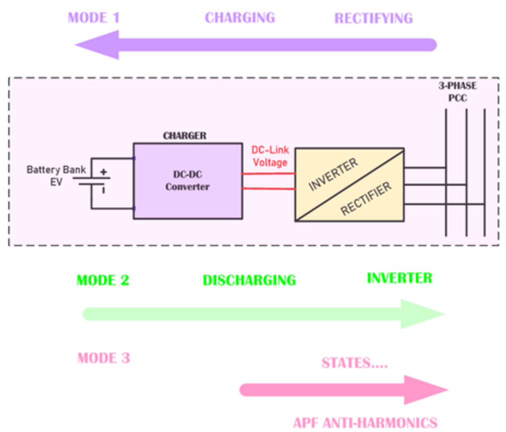

Figure 2: Different modes of operation of dc-dc converter

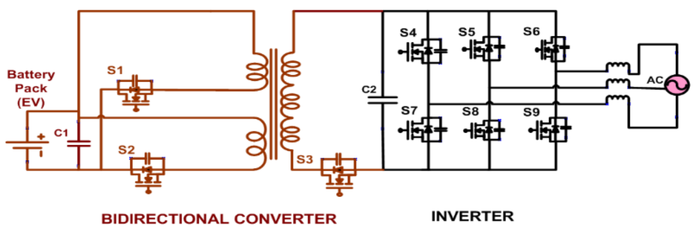

Figure 3: Proposed EV battery charger system.

The proposed design enhances the advanced power quality capacity and simplifies the structure without the large amount of switching devices in the EV battery charger applications as shown in Figure 3 and Figure 4. The bidirectional flyback converter proposed in this research in the EV battery charger. The proposed bidirectional flyback converter consists of a main transformer T with turn ratio n and main switches S1, S2, and S3. The circuit is designed to operate in bi-directional modes. During V2G, the bidirectional converter will step-up the low battery bank voltage to high dc link voltage and provide it at the input of inverter. The converter is specially designed to provide high battery bank current value at the input of the inverter. Similarly, in the Grid to Vehicle G2V mode, the bidirectional converter steps down the dc link voltage to low battery bank voltage. All the bidirectional operation is performed with a reduced number of switches.

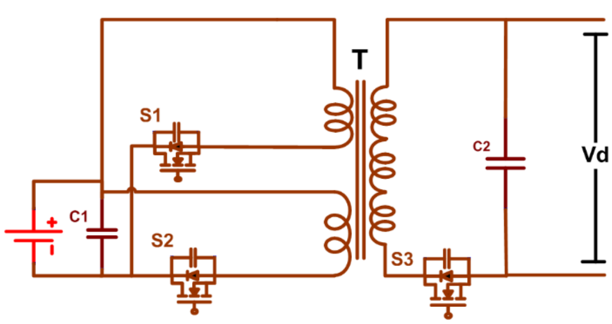

Figure 4. Proposed Bidirectional dc-dc converter.

B. Assumptions:

Following are the assumptions made to justify the analysis of the bidirectional flyback converter.

1. All the components in the proposed circuit are ideal.
2. During the flow of power from Battery bank to Inverter, which is the forward mode, the switch S1 & S2 acts as a controller whereas the switch S3 becomes the rectifier. Hence in reverse mode i.e (from grid to Battery bank), switch S3 becomes the controller and switch S1 & S2 acts as a rectifier.
3. It is noted that in both the mode, i.e. forward mode and backward mode, the proposed bidirectional flyback converter can function as buck–boost converter. However, in this research it is assumed that in the forward mode bidirectional flyback converter operate as boost and act as buck in the reverse mode.
4. Since the proposed converter is in a symmetrical structure, the working of the converter is explained in the forward mode only.
5. The proposed bidirectional flyback converter works only in the continuous conduction mode CCM.
6. It is assumed that during one switching cycle the magnetizing inductance of the transformer T is so large that its current is constant.
7. In EVs, Battery Management System BMS is one of the important components in lithium-ion-batteries. It is considered to improve the lifespan of the EV battery. A smart battery management system can use data to estimate the battery state of charge SoC to improve its performance. SoC, State of Charge specifies the battery's available capacity to avoid overcharging or discharging the battery pack.
8. The research suggests maintaining the battery state of charge SoC within the range of 20% to 85% to prolong the battery lifespan / life quality.

C. System analysis of proposed Bidirectional dc-dc converter system

1) V2G Mode of operation:

V2G mode becomes active when the SoC of the battery bank is more than 70%. During peak demand, the power from the battery pack is injected into the grid. Figure 5a, clearly explains that the switch S1 and S2 are turned ON during sub interval 1 whereas the switch S2 is turned OFF during the same interval. In this case the battery bank energy is stored in the magnetization inductor L_m of the circuit. Whereas in subinterval 2, Figure 5b the switch S1 and S2 are turned OFF and the switch S3 is turned ON. In the latter case, the stored energy in the magnetization inductor is effectively transferred to the secondary winding of the transformer to provide power at the DC link.

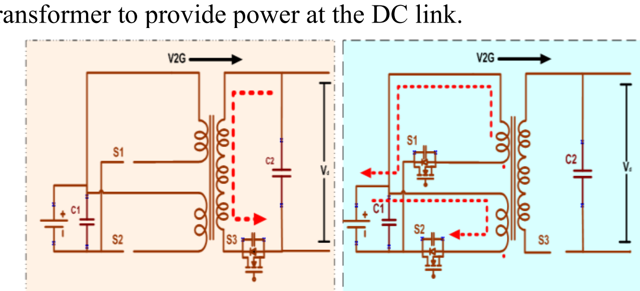

(a) **(b)**

Figure 5. V2G mode of operation.

2) G2V Mode of operation:

When the EV battery SoC is less than 30%, the battery needs to be charged. Therefore, this mode of operation will provide power from the grid into the battery bank. As shown in Figure 6a, the switch S1 and S2 are turned OFF and the switch S3 is turned ON in the subinterval one. In subinterval 1, the magnetization inductor L_{m2} is energized by the DC link voltage maintained by the converter operating as a rectifier. Whereas in subinterval two, Figure 6b, the switch S1 and S2 are turned ON and the switch S3 is turned OFF. During this time, the battery bank is charged by the primary winding of the transformer from the stored energy in the magnetization inductor.

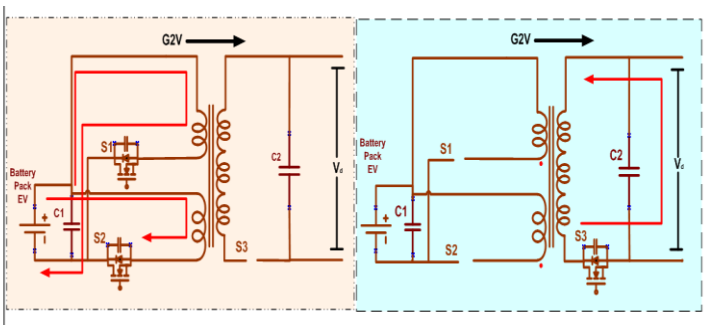

(a) (b)

Figure 6. G2V mode of operation.

D. Operation of Bidirectional High current density dc-dc converter in CCM Mode

The proposed bidirectional high current density dc-dc converter is specially designed to sustain high current with low voltage form of the battery bank thus mostly suits the given application. Besides, it is controlled by using the well-known Model predictive control and most importantly with reduced switch count, reduced complexity, and low cost etc.

1) Analysis of CCM Mode:

The switching stages of a proposed dc-dc converter in CCM Mode of operation, when the MOSFET switch is turned ON, the voltage across the primary winding of the inductor transformer is given by the input voltage which is the battery voltage v_{bat}. The primary current i_{pr} and the magnetic flux in the transformer increases, causing energy to store in the primary winding N_P of the transformer. As a result, the voltage v_{sec} induced in the secondary winding N_s is negative which makes the diode D reversed-biased. As the secondary current i_{sec} is zero , it is assume that the primary current also need to be zero, so $i_{pr}(t)= \frac{Ns}{N_p} \; i_{sec}(t)$. the input current charged the magnetizing inductance as $i_{in}(t)= i_m(t)$. This results in a strong DC component in the magnetizing current.

$$v_{bat} = v_m(t) = L_m \frac{d_i m}{dt}, 0 \le t \le DTs \quad (1)$$

During the first switching stage of the CCM mode, we get the magnetizing current as

$$i_m(t) = i_m(0) + \frac{Vin}{L_m} t, 0 \le t \le DTs \quad (2)$$

And reaches the peak value at the end of the first topology.

$$i_m, max = i_m(0) + \frac{Vin}{L_m} DTs \quad (3)$$

The polarities of the voltages across the primary and the secondary winding is defined as

$$v_{pr}(t) = v_{in}, \; V_{sec}(t) = 2(\frac{Ns}{N_p})\, v_{pr}(t) = 2(\frac{Ns}{N_p})\, v_{bat} \quad (4)$$

Where the diode voltage v_D is given as

$$v_D = -[\, V_{sec}(t) + V_{dc\ link}\,] = -[\, 2(\frac{Ns}{N_p})\; v_{bat} + v_{dc\ link}\,] \quad (5)$$

The output capacitor provides energy to the output load which is the dc link. When the switch is OFF, the energy is transferred to the secondary windings and the transformer demagnetizes causing the primary current and magnetic flux to drop down/ decrease. The secondary current does not ramp all the way to zero amps. therefore $i_{pr}(t)$=$i_m(t)$. As the secondary voltage v_{sec} is positive, it forward biases the diode and allows the current to flow through the secondary winding. The stored energy from the secondary winding recharges the capacitor and supplies the load i.e. the dc link. The next switching cycle begins rapidly before the current is completely depleted.

$$V_{sec}(t) = -\, V_{out} \quad ; \quad v_{pr}(t) 2(\frac{Np}{N_s})\; V_{sec}(t) = -2(\frac{Np}{N_s})\; V_{dc\ link}, DTs \le t \le Ts \quad (6)$$

Voltage across the transistor will be,

$$V_{DS}(S) = V_{bat}\text{-}V_{pr}(t) = V_{bat} + 2(\frac{Np}{N_s})\; V_{dc\ link} \quad (7)$$

From equation,

$$V_m(t) = V_{pr}(t) = -2(\frac{Np}{N_s})\; V_{dc\ link} \quad DTs \le t \le Ts \quad (8)$$

It shows that the magnetizing inductance will be discharged by the current:

$$i_m(t) = I_{m,\max} - \frac{1}{Lm}\, 2(\frac{Np}{N_s})\; V_{dc\ link}(t - DTs) \quad DTs \le t \le Ts \quad (9)$$

Now the diode will carry the reflected too secondary primary current,

$$i_D(t) = i_{sec}(t) = 2\frac{Np}{N_s}\, [\, I_{m,\max} - \frac{1}{Lm} \frac{Np}{N_s}\; V_{dc\ link}(t - DTs)\,] \quad (10)$$

The working purpose of the isolation element is like a coupled inductor in flyback converter from the forward converter. During the first cycle of the switch, the magnetizing inductance is responsible for storing the input energy, hence there is no energy transferred across the load. During the second switching cycle when there is no input battery voltage, this energy is successfully transferred to the load (dc link). This special isolation element acts as a buck-boost converter because of which it eliminated the need of reset mechanism for the magnetizing the inductance and makes the coupled inductor as simple as possible. According to the volt-second balance on magnetizing inductor, with $v_{bat}(t) = v_{bat}$ For on-topology duration DTs, and $V_m(t) = - 2\frac{Np}{N_s}\ V_{dc\ link}$ and for off-topology duration $(t - D)Ts$ we get:

$$V_{bat}\, DTs + (- 2\frac{Np}{N_s}\ V_{dc\ link})\,(1 - D)Ts = 0 \tag{11}$$

$$V_{dc\ link} = \frac{D}{1-D}\, 2(\frac{Ns}{N_p})\ \ V_{bat} \tag{12}$$

In the hypothesis of 100% efficiency, the ratio between the average input and output current is given as,

$$\frac{i_{bat}}{i_{dc\ link}} = \frac{V_{dc\ link}}{V_{bat}} = \frac{D}{1-D} . 2 . \frac{Ns}{N_p}$$

From above received formulas we can find equations for the transistor and diode voltage stress,

$$V_{DS}(S) = V_{bat} + \frac{Np}{N_s}\ V_{dc\ link} = V_{bat} + \frac{Np}{N_s} \frac{D}{1-D} . 2 . \frac{Ns}{N_p}\ V_{bat} = \frac{1}{1-D} V_{bat} = 2\frac{Np}{N_s}\ \frac{1}{D}\ V_{dc\ link} \tag{13}$$

$$V_{DStress} = \frac{Ns}{N_p}\ V_{bat} + V_{dc\ link} = 2\frac{Ns}{N_p}\ (\frac{1-D}{D}\ \frac{Np}{N_s}\ \frac{1}{D}\ V_{dc\ link}) + V_{dc\ link} = \frac{1}{D}\ V_{dc\ link} \tag{14}$$

It is noted that during the first switching cycle, the input current is equal to the magnetizing current and during the second switching cycle it is equal to zero. We can easily calculate the average input current.

$$I_{bat} = \frac{1}{Ts} \left[\int_0^{DTs} i_m(t)\, dt + \int_{DTs}^{Ts} 0\, dt\right] = \frac{1}{Ts} [\ I_m DTs + 0(1\text{-}D)\, Ts\ ] = \mathrm{D}\, I_m \tag{15}$$

Where I_m donates average of the magnetizing current $i_m(t)$,

$$I_m = \frac{I_{bat}}{D} = \frac{D}{1-D}\, 2\, \frac{Ns}{N_p}\ V_{dc\ link} \tag{16}$$

It is observed that the transistor and diode voltage stress are comparatively small according to their actual values of the $V_{bat}, V_{dc\ link}$ and $\frac{Ns}{N_p}$ to a forward converter. In a steady state switching cycle the ripple of the magnetizing current can be obtained as,

$$I_{m,max} = I_m(0) + \frac{V_{bat}}{L_m} DTs \tag{17}$$

$$I_{m,min} = I_m(0) = I_m(Ts) = I_{m,max} - \frac{1}{Lm}\ 2\frac{Np}{N_s}\ V_{dc\ link}\ (1\text{-}D)\, Ts \tag{18}$$

$$\Delta Im = I_{m,max} - I_{m,min} \tag{19}$$

$$= \frac{V_{bat}}{L_m} DTs = \frac{1}{Lm}\ \frac{Np}{N_s}\ V_{dc\ link}\ (1\text{-}D)\, Ts \tag{20}$$

Hence average magnetizing current is $Im = \frac{1}{1-D}\frac{Ns}{N_p}\ I_{dc\ link}$. We can easily get the maximum and the minimum magnetizing current as,

$$I_{m,max} = I_m + \frac{\Delta Im}{2} = \frac{1}{1-D}\, 2\, \frac{Ns}{N_p}\ \ I_{dc\ link} + \frac{1}{2} \frac{1}{Lm}\, 2\, \frac{Np}{N_s}\ V_{dc\ link}\, (1\text{-}D)\, Ts \tag{21}$$

$$I_{m,min} = I_m - \frac{\Delta Im}{2} = \frac{1}{1-D}\, 2\, \frac{Ns}{N_p}\ \ I_{dc\ link} - \frac{1}{2} \frac{1}{Lm}\, 2\, \frac{Np}{N_s}\ V_{dc\ link}\, (1\text{-}D)\, Ts \tag{22}$$

5.2 Small signal model of the proposed high current density dc-dc converter

The small-signal model for the high current density dc-dc converter is same as that of the buck-boost converter. It is necessary to consider the number of turns ratio of the coupled inductor, $\frac{Ns}{N_p}$. according to the Figure 7 (a), and Figure 7 (b) in which the parasitic resistances are ignored, we can get the space-state equations as follows.

$$L_m \frac{di_m}{dt} = v_{bat};\ \ C\frac{dv_{dc\ link}}{dt} = -\frac{1}{R}\, v_{dc\ link}\ ;\quad 0 \le t < DTs \tag{23}$$

$$L_m \frac{di_m}{dt} = \frac{Np}{N_s}\ V_{dc\ link}\ ;\ ;\quad C\frac{dv_{dc\ link}}{dt} = \frac{Np}{N_s}\ i_m - \frac{1}{R}\, v_{dc\ link}\ ;\quad DTs \le t < Ts \tag{24}$$

We get the average space-state equation as

$$L_m \frac{di_m}{dt} = d(t) v_{bat}(t) - [1 - d(t)\,]\, 2\frac{Np}{N_s} V_{dc\ link}(t) \tag{25}$$

$$C\frac{dv_{dc\ link}}{dt} = [1 - d(t)\ ]\ 2(\frac{Np}{N_s})\ i_m(t) - \frac{1}{R}\, v_{dc\ link}(t) \tag{26}$$

To get the exact average state-space equation of the buck-boost power stage, we will not consider the turns ratio $\frac{Ns}{N_p}$, and replace the L_m by the inductance L as if in a buck-boost converter and $i_m(t)$ by $i_L(t)$. Fig(below) shows the transformed average small-signal model of the converter. Where r_L denotes the parasitic resistance of the primary winding of the coupled inductor. The polarity of $V_{dc\ link}(t)$, $V_c\,(t)$ are transformer inversed. We can now easily get the transfer function of the flyback converter by applying the same method of alterations to achieve graphical average model. One of the main purposes is to find the open loop input impedance $z_{in}(s)$ of the proposed dc-dc converter converter. It is noted that the input segment of the average model is not influenced by the turn's ratio $\frac{Ns}{N_p}$, of the coupled inductor. Which shows that the proposed dc-dc converter holds the same small input impedance as for the buck-boost power stage.

$$z_{in}(s) = \left.\frac{\hat{v}_{bat(s)}}{\hat{I}bat(s)}\right|_{\hat{D}(s)=0,\ i_{dclink(s)}=0} = \frac{R}{M^2} \tag{27}$$

The flyback converters are successfully used in AC-DC rectifiers with a fair power factor. Due to the advantage of flyback converter with minimum number of elements, DC isolation and the benefit of its multiple outputs it is often preferred to be used in low power rectifiers. There are a few disadvantages of flyback converter i.e. high pulsating input and output currents and high level of magnetizing and switches current stress most specifically operated in the DCM mode.

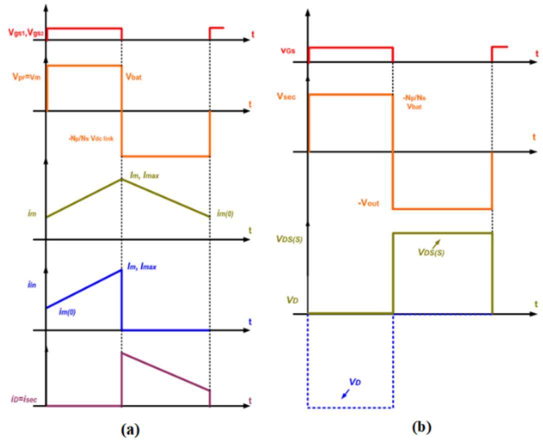

Figure 7 (a) and (b). Steady state waveform of a proposed converter in CCM mode.

E. Control

The operation of the system is completed by introducing the close loop control of each part of the system. The high current density bidirectional dc-dc converter is controlled using model predictive control. This bidirectional converter ensures regulated dc voltage at the battery bank voltage at the vehicles side as well as regulated voltage at dc-link. Similarly, the control of the inverter is ensured using the model predictive control for the voltage source inverter. Moreover, the active power filter control technique is also ensured using the same inverter during mode 3 operation. The inverter proposed is the two-level voltage source inverters (2L-VSI) and the circuit diagram with control techniques is well demonstrated in Figure 8.

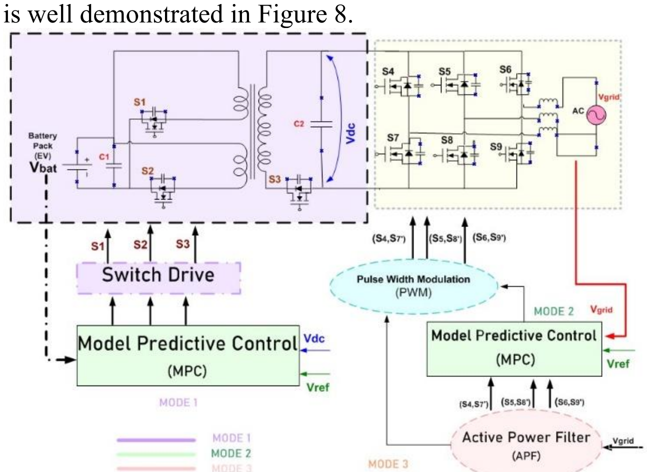

Figure 8. Model Predictive Control for the VSI.

1) *Model Predictive Control of High Current density bidirectional dc-dc converter*

The batteries of the vehicles are successfully used to overcome the power gap generated by the changes in the load demand in the form of voltage sags. Batteries of the vehicles work by switching of the bidirectional dc-dc converter to regulate the power supplied or absorbed by the vehicle's batteries. It is therefore very important to keep track of the effects of different switching states on the amount of power supplied or absorbed. Figure 8 shows the brief circuit of the bidirectional dc-dc converter where the battery voltage is represented by v_B, v_{dC} shows the dc bus voltage, the battery output current is represented by I_{bat}, whereas the I_B is the battery input current. The low voltage (LV) bus and high voltage (HV) bus are the two sides of the converter. They are connected to the battery and the dc bus. S1 & S2 and S3 are the switches which are driven by a set of complementary signals. During the discharge mode of the battery, power is supplied, and the Bidirectional dc-dc converter operates in the buck mode as shown in Figure 6(a). However, in the charging mode of the battery the power is absorbed, and the bidirectional converter operates in the buck mode as shown in Figure 6(b). Figure 6(a) and Figure 6(b) is the combination of representing I_B in boost mode as a positive current.

$$\begin{cases} s_2 = 1 \quad & s_1 = 0\colon L_B \dfrac{dI_B}{dt} = v_B \\ s_1 = 0, \quad & s_1 = 1\colon \ L_B \dfrac{dI_B}{dt} = v_{B-v_{dC}} \end{cases} \tag{28}$$

The discrete-time model for a sampling time Ts can be expressed as:

$$\begin{cases} s_2 = 1, \quad & s_1 = 0\colon \quad I_B(k+1) = \dfrac{T_s}{L_B} v_B(k) + \\ s_1 = 0, \quad & s_1 = 1\colon \quad I_B(k+1) = \dfrac{T_s}{L_B}(-v_{dc}(k) \end{cases} \tag{29}$$

To calculate the cost function for charging and discharging the battery, following equation can be used to regulate the battery current.

$$J_C = |I_B^* - I_B(k+1)|$$
$$S \cdot t \cdot SOC_{min} \leq SOC \leq SOC_{min},\ I_B \leq |I_{b\,\text{at}-rated}| \tag{30}$$

The battery current is represented by $I *_B$ which is maintained according to the electricity prices in grid connected operations which is explained briefly in section IV. The flow of the current is demonstrated in between the BESS, the renewable energy sources (RES) and the rest of the microgrid (ROM). The power balance between the microgrid is maintained by a proper charging and discharging of the BESS. By applying Kirchoff's current law (KCL) to the above phenomena, the relationship of the currents can be expressed as:

$$I_{Dc} = I_{RES} - I_C - I_{ROM} \tag{31}$$

In the equation (31), I_{DC} represents the current supplied or absorbed by BESS, IRES represents the current from the renewable energy sources, I_C stand for the flowing current through the dc-side capacitor and I_{ROM} denotes the current following into dc loads and the inverter. As a result, the $(k+1)^{\text{th}}$ is the power required by BESS to keep the power balance within the microgrid which can be calculated as

$$P *_{BESS}(k+1) = |I_{DC}(k+1).v^*{}_{dc}| \tag{32}$$

where v_{dc^*} is the voltage reference for dc bus.

Figure 8 shows that the Vdc which is the dc side voltage can be related directly to the effects of capacitor C_2. For such capacitors, the capacitor voltage can be determined by the rate of current flowing through it, that is $I_C = \frac{C_2\, dv_{dC}}{dt}$. This equation explains that the change of dc side voltage V_{dc} can result in corresponding change of the current IC. Although V_{dc} is controlled by its rated value V_{dc}*, there is always a deviation between Vdc and Vdc* followed by a linear change within a very short period. The value of I_C is determined by the Vdc gap which is not large enough to which a reference prediction horizon N is introduced [47]. It explains that Vdc(k) could be higher, represented by $(V_{dc}(k)a)$ or lower $(V_{dc}(k)a)$ than the rated dc voltage Vdc*. This process results in $I_C\ (k)a$ steps down or $I_C\ (k)b$ steps up and N means Vdc(k) in V_{dc}* in N steps. taking next instant $k+1$ into account, it can be obtained that [47, 48].

$$\frac{V_{dc}(k) - V_{dc}(\,k+1)}{1} = \frac{V_{dc}(k) - V_{dc}\,*}{N} \tag{33}$$

$$V_{dc}(\,k+1) = V_{dc}(k) + \frac{1}{N}\left(v_{dc^*} - V_{dc}(k)\right) \tag{34}$$

Similarly, according to the Euler's forward-difference law

$$I_c(k+1) = \frac{c_2}{T_s}\left(V_{dc}(k+1) - V_{dc}(k)\right) = \frac{c_2}{NT_s}\left(v_{dc^*} - V_{dc}(k)\right) \tag{35}$$

where N represents as an integer coefficient used to limit the capacitor's current. According to the equation (31) and (35), BESS current can be predicted as,

$$I_{Dc}(k+1) = I_{RES}(k) - I_c(k+1) - I_{ROM}(k) \tag{36}$$

in steady state, there is slow change in the battery voltage v_B (i.e. $v_B\ (k) = v_B(k+1)$) and the equality of battery output current I_{bat} and inductor current I_B, the output power of the battery can be predicted as,

$$P_{bat}(K+1) = |I_B(k+1).\,V_B(K)| \tag{37}$$

The BESS provides the amount of power required to keep a power balance with the microgrid supplied by the buck boost converter batteries. Therefore, minimizing the cost function,

$$J_p = |P^*_{BEss}(k+1) - P_{bat}(K+1)| \tag{38}$$

$$S \cdot t \cdot SOC_{min} \le SOC \le SOC_{max},\ I_B \le |I_{b\,\mathrm{at}-rated}| \tag{39}$$

During the grid-connected mode to control the charging or discharging current as demonstrated in Figure 9. The battery voltage and current operate with the actual dc bus voltage to manage the calculated battery current $I_b(k+1)$ according to equation (26). To control the function of the buck boost converter the switching behavior should be reduced equation (29). BESS maintains a constant dc-bus voltage in the islanded mode as shown in Figure 10. According to equation (32), (33) and (34), to calculate the BESS power required IRES which is the renewable energy sources output current, IROM which is the current following into dc loads and the inverter for ac loads, Vdc actual dc-bus voltage and reference voltage Vdc* respectively. The battery current $I_b(k+1)$ is predicted by the voltage and current off the battery, together with the actual dc-bus voltage, to two possible values of $P_{bat}(K+1)$ according to equation (29) and (34). The reduced switching behavior will be chosen to control the buck-boost converter.

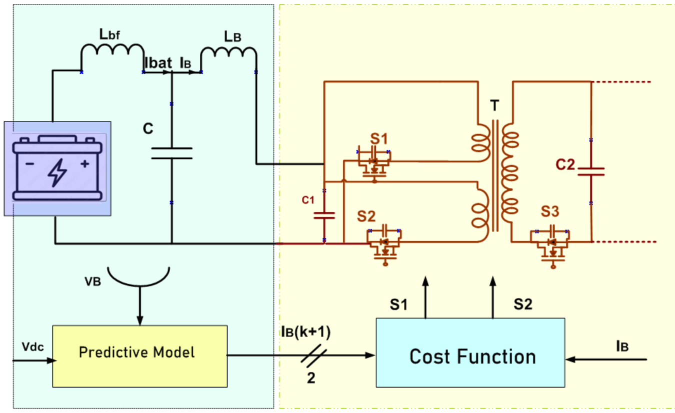

Figure 9. Block diagram of MPCP to control Buck-Boost Converter, operation in Grid connected mode.

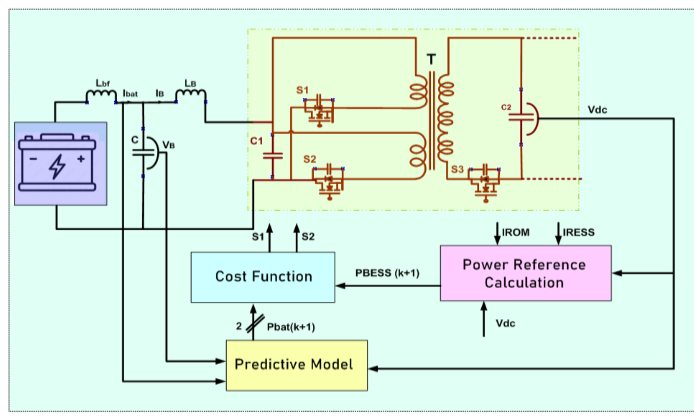

Figure 10. Block diagram of MPCP to control Buck-Boost Converter, operation in islanded mode.

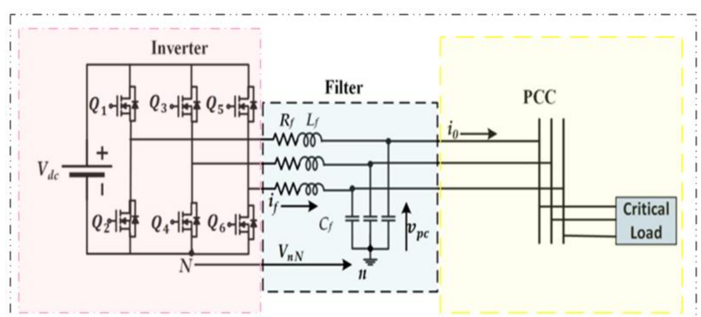

Figure 11. Two level three phase VSI.

Figure 11 explains a single inverter together with its LC filter is connected for system modelling. To achieve a good performance of the controller, errorless and well-designed mathematical modeling system of inverter and filter are required. As noticed in the Figure. 11, the v_{PC} represents the output voltage at PCC, i_0 shows the output current of the inverter, where L_f is the filter inductance, C_f is the filter capacitance, and v_{dc} vdc is the capacitor DC link voltage. However, s_x, s_y, s_z are respectively the legs of the converter. Perhaps, the harmonics generated by the two-level voltage source inverters (2L-VSI) are lessened by the LC Filter whose modeling has been shown in any frame of reference [49]. The kind of modeling performed in this paper presents is VSI modelling in an αβ frame of reference. following assumptions are made to implement the proposed control idea i.e., the system conditions were balanced, and zero sequence components were neglected. Implementing the clark transformation, all three-phase currents and voltages were transformed into the stationary frame of reference.

$$\bar{v} = v_\alpha + jv_\beta = \bar{T}\left[v_x v_y v_z\right]' \tag{40}$$

$$\bar{i} = i_\alpha + ji\beta = \bar{T}\left[i_x i_y i_z\right]' \tag{41}$$

$$\bar{T} = \frac{1}{3}\left[1e^{j\frac{2}{3}\Pi} \quad 1e^{j\frac{4}{3}\Pi}\right] \tag{42}$$

Figure 12 explains the switching arrangements of the VSI model. The legs of the VSI model is receiving three gating pulses such as,s_x ,s_y, s_z [50, 51].

$$s_x = \begin{cases} 1, if\ Q1\ is\ ON\ and\ Q_4\ is\ OFF \\ 0,\ \ if\ Q1\ is\ OFF\ and\ Q_4\ is\ ON \end{cases} \cdots \tag{43}$$

$$s_y = \begin{cases} 1, if\ Q_2\ is\ ON\ and\ Q_5\ is\ OFF \\ 0,\ \ if\ Q_2\ is\ OFF\ and\ Q_5\ is\ ON \end{cases} \tag{44}$$

$$s_z = \begin{cases} 1, if\ Q_3\ is\ ON\ and\ Q_6\ is\ OFF \\ 0,\ \ if\ Q_3\ is\ OFF\ and\ Q_6\ is\ ON \end{cases} \cdots \tag{45}$$

The voltage vectors in two level VSI are almost up to eight (2^3). The voltage at the output of the inverter legs can be obtained by taking the product of the state of the representative leg and dc link voltage.

$$v_x N = Sx \cdot v_{dc} \tag{46}$$

$$v_y N = Sy \cdot v_{dc} \tag{47}$$

$$v_z N = Sz \cdot v_{dc} \tag{48}$$

Kirchhoff's voltage law can be used to obtain common mode voltage VnN,

$$v_n N = \frac{v_x N + v_y N + v_z N}{3} \tag{49}$$

Hence inverter phase voltage is calculated as,

$$v_{xn} N = v_x N - v_n N \tag{50}$$

$$v_{yn} N = v_y N - v_n N \tag{51}$$

$$v_{zn} N = v_z N - v_n N \tag{52}$$

Figure 13 shows that v_0 and v_7 lie at the origin and represents zero vector. It also explains the position of all possible voltage vectors in the αβ frame [50].

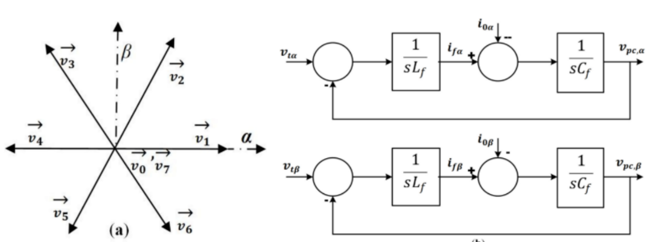

Figure 12. (a) Possible voltage vector of 2L-VSI. (b) Equivalent Filter model in the (α,β) frame.

Space Vector		Switching Vector	On-State Switch	Vector Placing
Zero vector	$\vec{v}_{0,7}$	$[PPP]$ $[OOO]$	Q_1, Q_3, Q_5 Q_4, Q_6, Q_2	$\vec{v}_0 = 0$ $\vec{v}_7 = 0$
Active vector	$\vec{v}_1$	$[POO]$	Q_1, Q_4, Q_6	$\vec{v}_1 = \frac{2}{3}v_{dc}$
	$\vec{v}_2$	$[PPO]$	Q_1, Q_3, Q_6	$\vec{v}_2 = \frac{1}{3}v_{dc} + j\frac{\sqrt{3}}{3}v_{dc}$
	$\vec{v}_3$	$[OPO]$	Q_2, Q_3, Q_6	$\vec{v}_3 = -\frac{1}{3}v_{dc} + j\frac{\sqrt{3}}{3}v_{dc}$
	$\vec{v}_4$	$[OPP]$	Q_2, Q_3, Q_5	$\vec{v}_4 = -\frac{2}{3}v_{dc}$
	$\vec{v}_5$	$[OOP]$	Q_2, Q_4, Q_5	$\vec{v}_5 = -\frac{1}{3}v_{dc} - j\frac{\sqrt{3}}{3}v_{dc}$
	$\vec{v}_6$	$[POP]$	Q_1, Q_4, Q_5	$\vec{v}_6 = \frac{1}{3}v_{dc} - j\frac{\sqrt{3}}{3}v_{dc}$

Figure 13: Switching arrangements of 2L-VSI.

2) Operating Principle of FCS–MPC

An FCS-MPC technique is proposed for the voltage control of an inverter explained well in Figure 14. The following are the basic principles of voltage MPC.

- In the beginning of every sampling time, the values of v_{PC}, i_f and i_0 are measured through sensors.
- The collected information/data is sent to the algorithm, which is defined by the starting point. From this point the algorithm predicts the future behavior of controlled variables. The prediction is performed for all possible voltage vectors successfully.
- The predicted values are then used to find the cost functions (CF) and a voltage vector to VSI. CF allows to solve multi-objective problems defined as

$$g_{GEN} = \sum_{i=t_k}^{tk+N-1} ||v_f e(\mathrm{i})||^2 + h_{lim}(i) + \lambda_{su} w^2(i) \tag{53}$$

Figure 14 shows the flowchart of the VMPC algorithm with a designed cost function in FCS–MPC in equation (53), $v_{fe(i)}$ is the predicted tracking error, $h_{lim}(i)$ is the limit current constraint, $sw^2(i)$ is used to minimize the switching frequency and controlled by weighting factor λu. Equation (53) can be explained as,

$$v_{fe}(i) = v_{f^*}(i) - v_f(i) \tag{54}$$

$$h_{lim}(i) = \begin{cases} 0, & if|if(i)| \leq i_{\max} \\ \infty, & if|if(i)| > i_{max} \end{cases} \tag{55}$$

$$sw(i) = \sum|(i) - u(i-1)| \tag{56}$$

The cost function in equation (57) is a charted form of equation (53) with N = 2. Its major function is to reduce the Euclidean distance at every sampling time. The proposed cost function in the paper explains the desired system behavior and is described as follows:

$$g_v = (\ v^*_{(pc)\alpha}(t_k+2) - v_{(pc)\alpha}(t_k+2))^2 + (\ v^*_{(pc)\beta}(t_k+2) - v_{(pc)\beta}(t_k+2))^2 \tag{57}$$

At the output voltage reference at $(t_k + 2)$ instant, $v^*_{(pc)\alpha}\ and\ v^*_{(pc)\beta}$ are its real and imaginary parts which are taken from the droop control part. Where, $v_{(pc)\alpha}$ and $v_{(pc)\beta}$ are the predicted output voltage. The predicted cost function provides a reduced voltage error and switching frequency of VSI. This shows the method used in this paper for reduced switching frequency. We can add additional constraints such as current limitations etc. but it can cause the tuning of weight coefficients and will create issues in the performance of the controller.

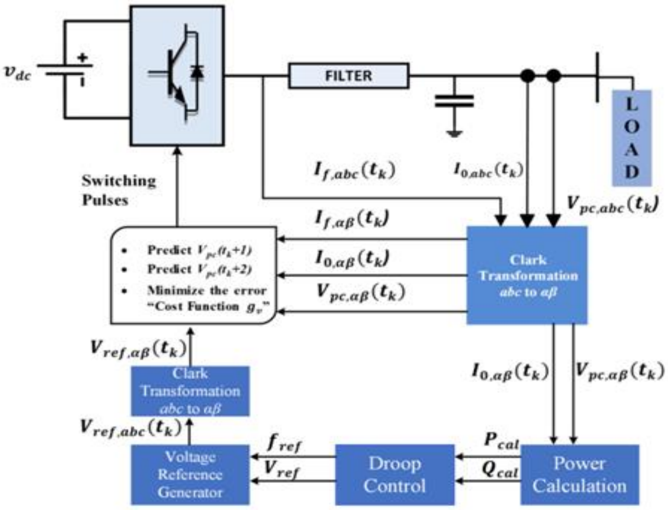

Figure 14. Block diagram of finite control set model predictive control (FCS-MPC) technique for UPS system along with droop control.

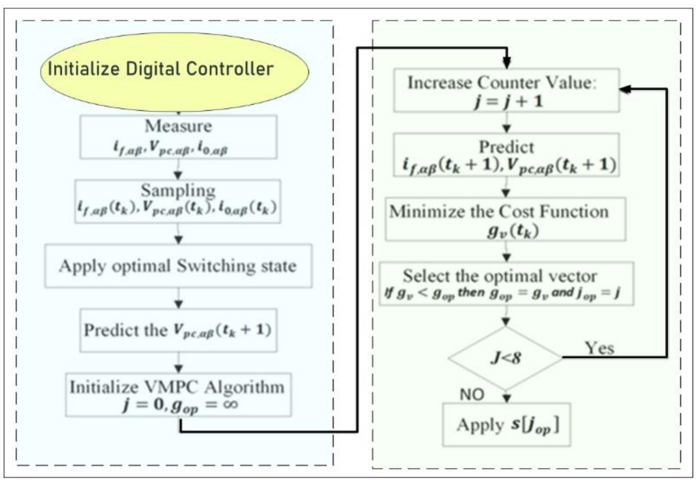

Figure 15. Flowchart of the V-MPC algorithm.

3) Switching Frequency Reduction Scheme

The use of the inverter in a backup storage system is to interface the battery bank with the output load. In this regard, switching frequency plays a vital role in reducing losses and is related to the low frequency and vice versa. In order, to achieve the low switching frequency, a two-step reduction technique is used.in one-step sampling technique for one period, eight vectors are exploited. To find the value of N=2 i.e. the prediction horizon, two voltage vectors are considered, one for the first sampling period and the other vector for second sampling period. Figure 16 (b), the total number of possible sequences of voltage vector (72) are used. It can be evaluated that the total number of possible sequences are 49.

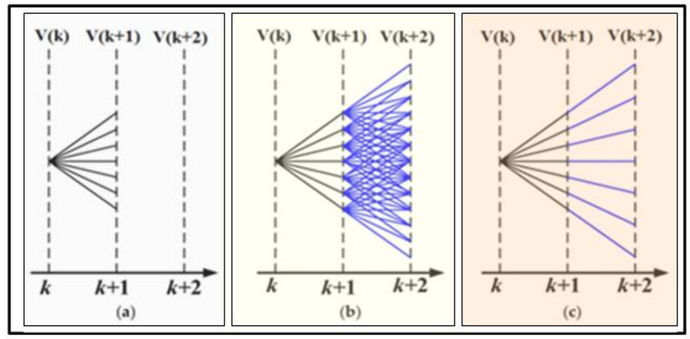

Figure 16. Vector representation of switching frequency. (a) N = 1 and (b) N = 2 are different voltage vectors during each sampling instant. (c) N = 2 taking same voltage vectors during two-sampling instants.

To solve the computational burden and control accuracy issues, a two -step prediction technique is used. The same voltage vector is used for the first and the second sampling period respectively [52]. It is clearly shown in Figure 16 (c), that only seven voltage vectors are used for two step prediction process. This technique came out to be successful for similar performance with less switching frequency. The voltage level can be predicted up to $t_k + 2$. Which means for two sampling instant eight possible voltage vectors can be used. This technique also helps in reducing the switching frequency of VSI and voltage ripple.

4) Active Power Filter Control

The major purpose of the APF controller is to remove the current harmonics and establish a steady and constant dc-link voltage. The working of the controller consists of three parts: APF system reference generator, phase lock loop (PLL) and dc-link voltage control as shown in Figure 17. The phase lock loop scheme provides a transient free locking to the rotating synchronous frame with the positive sequence of the three-phase supply voltages. The PLL scheme is helpful in controlling the reference voltage for VSI operation systems.

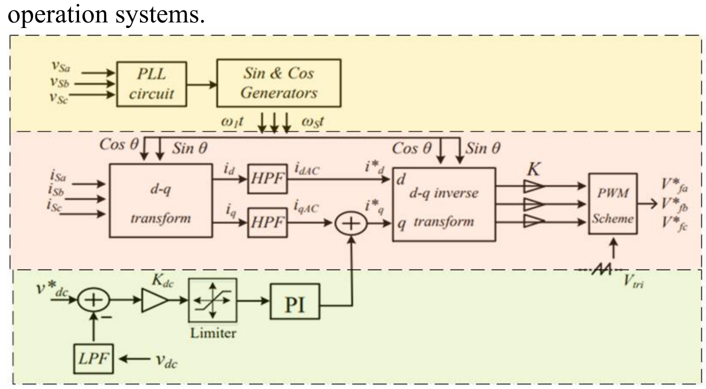

Figure 17: Overall system of the proposed SAPF

To avoid zero utility current and reduce the ripples in the output voltage waveform, an SPWM switching scheme is considered efficient and helpful to compensate the harmonic contents. With reference to the PWM switching scheme, the high-frequency triangular wave (V_{tri}) is compared to the modulation signal. The 3-phase supply current is converted into a 2-phase instantaneous active (i_d) and instantaneous reactive (i_q) currents at the fundamental frequency. Due to the three-phase system the zero sequence is ignored, providing ac voltage to compensate the system harmonics by the VSI. at the fundamental frequency (ω1 = 50 Hz), the active and reactive quantities are decomposed into dc and ac values respectively. Two second-order high-pass filters (HPFs) are designed to extract the ac current harmonics into (i_{dAC}) and (i_{qAC}), at the cutoff (50 Hz) frequency level [53]. The performance of the APF and dynamic voltage damping is affected by the HPF sample time delay [54]. The process ends with the regeneration of the supply harmonic current components by the inverse d-q transformation. The parameters of the APF are dependent upon the value of gain (K). for proper switching gate signals of the PWM inverter the reference voltage,(V_{AF}^*) of each phase (v_{Af}, v_{Bf}, v_{Cf}) is amplified by the gain (K), in equation (58).

$$V_{AF}^* = K \times iF_{abc} \tag{58}$$

III. RESULTS AND DISCUSSIONS

A. System Particulars

To assess the effectiveness of the suggested system, a detailed computer simulation is conducted to implement all its components. Table 2 outlines the parameters of the proposed system, with each portion designed in such a manner that it justifies according to the overall system rating. This work explains the control part for the battery charger and battery discharger, the rectifier and the inverter in the system are executed using MATLAB/Simulink. Keeping in view the backup time for the load connected two parallel batteries of 24V/35 Ah are used as back-up for storage system.

Table 2. Requirement of the proposed system

Parameters	Symbol	Value
Grid Voltage	V_G	400V
Grid Frequency	f_r	50Hz
Battery Bank of Vehicle	VB	200V
Maximum Power Output	Po, max	5 kVA
DC-link Voltage	V_{DC}	650V

1) AC-DC Inverter in three-phase

The effectiveness of the inverter control system proposed is verified through simulation using MATLAB-Simulink. Table 2, and Table 3, show the detailed parameters and specifications of the circuit and system control. The selection of the α value considers the circuit detail parameters. load tests are conducted in various scenarios, including grid-connected mode, unbalanced conditions, and both linear and non-linear three-phase uncontrolled diode rectifiers. The non-linear loads are modeled according to the IEC 62040-3 standards, featuring a 0.3Ω of resistance at the input in series, 4700uF of capacitor (C) and 40Ω of load resistance in parallel. The evaluation of results encompasses quick response, Evaluation of harmonic distortion, considering both linear and non-linear loads and steady-state error of the system. Taking into consideration the parameters of control, for linear loads the value of the total harmonic distortion is 0.4% whereas for non-linear loads is 1.25%.

Table 3. Requirement of the proposed system

The need for the external power source can be eliminated by extensive absorption of the active power increasing the dc-link voltage. To keep the active filter, save from damage, the reactive dc current (iq_{DC}) is injected into the quadrature axis. At this point, a proportional integral (PI) controller is used at the required voltage level of the PWM inverter for the comparison of the reference signal with the detected dc-link voltage to get final voltage reference. The PI controllers are found successful in maintaining the harmonics current time derivatives for filtering operation. Although, the voltage reference is kept higher than the topmost value of the ac supply voltage. Hence, the values of the proportional (k_P)and integral (k_I) gain are defined as 0.2 Ω −1 and 31 Ω −1 [55].

Parameters	Symbol	Value
Grid Voltage	V_G	400V
Grid Frequency	f_r	50Hz
Battery Bank of Vehicle	V_B	200V
Maximum Power Output	Po, max	5 kVA
DC-link Voltage	V_{DC}	650V

Table 4. Specifications of the single-phase inverter

Parameters	**Symbol**	**Value**
Switching Frequency	f_{sw}	20 kHz
Switches	S_5~S_8	SPP11N60C3
Output Filter Inductor	L_f	840μH
Output Filter Capacitor	C_f	6.6μF
Cutoff Frequency	f_{cut}	17,00Hz
Load resistance	R_L	40Ω
Power Rating	P*o*	1kVA

2) Grid- Connected Mode

In grid-connected mode, the system maintains stable voltage and frequency, aligning with the main grid references. Consequently, the need to utilize controllers for voltage and frequency becomes unnecessary. Instead, a PQ controller is employed for precise sharing of power, particularly beneficial when a Distributed Generator (DG) functions as a grid-feeding inverter. The response time of the PQ controller is faster compared to droop control in this scenario. During grid-feeding, current is introduced into the grid to fulfill the load demands. Different conditions occur such as DGs generate more power than the load requirements than excess power will flow to utility gird and other case is that DGs produced less power than load demand, extra power will be supplied by the utility power grid to fulfill the load demand. Different test simulations are performed to show the robustness of DPMPC.

B. Inverter connected with grid system

A single inverter is connected in parallel with grid at PCC and RL Load is connected. This case shows the capability of DPMC to deliver flexible power between VSC and grid.

1) Balanced linear load

In this study a linear RL load relates to a single DG at the PCC. Table 2 shows the load and DG along with filter parameter. Figure 18 illustrates the (a) waveform at the output voltage, (b) the current waveform. Figure 18 (c) and figure 18 (d) show the output active and reactive power of DG under linear load tracking the reference. The DG output voltage and current waveform is sinusoidal and in phase with grid. Likewise, Figures. 19 present the THD of voltage and current. THD was found by using the built-in algorithm fast Fourier transform (FFT) in MATLAB. THD in current is 2.91% which is according to Institute of Electrical and Electronics Engineers (IEEE) codes and THD of voltage is 0.68%. It is also less than 3% for isolated systems. Voltage waveforms are stable which shows the robustness of proposed controller under linear load.

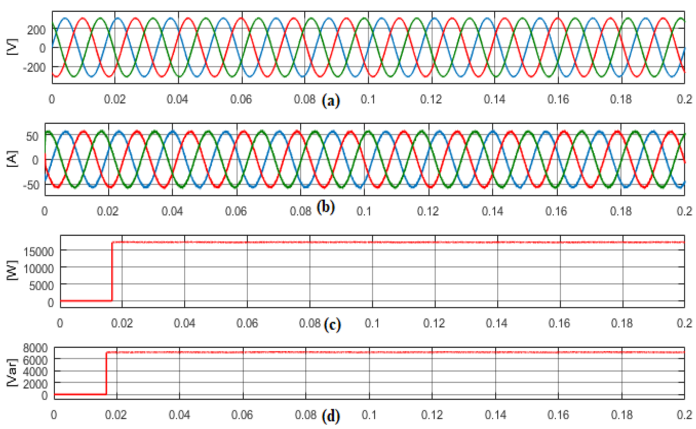

Figure 18. Simulation of control scheme with linear load. (a) Fundamental voltage amplitude: 318V (b) load current waveform (c) VSC active power. (d) VSC reactive power.

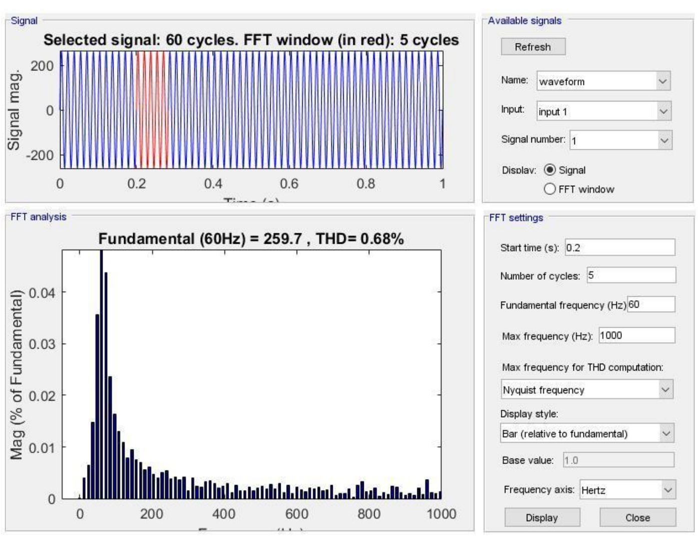

Figure 19. Grid connected mode for FFT analysis of Inverter Output Voltage

2) *Modification in the reference values for the (P) and (Q) power in a single (DG).*

At this point, the voltage source converter (VSC) functions as a grid-feeding system. for active power (P), at time t=0.1 there is a shift in the reference value ranging from 18 kW to 28 kW. Where the change in the reactive power reference value is from 7 kVar to 10 kVar. As shown in Figure 20, at time t=0s, the current of the DG increases to fulfill new demand of active and reactive power. The minimum time required is less than 0.02 seconds, for the power to stabilize at the new reference.

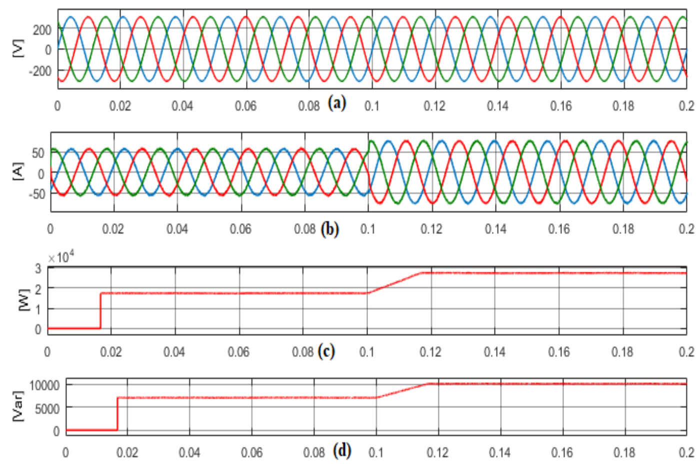

Figure 20. Simulation of the proposed control system (a) Voltage amplitude: 318V (b) load current waveform (c) VSC active power. (d) VSC reactive power.

3) *For linear Load*

To illustrate the parallel operation of DGs under linear load in islanded mode of MG, different simulations are performed to check the system response in parallel operation. the voltage, current, active, and reactive power under linear loads is represented in Figure 21 and Figure 22. Droop control is implemented to achieve precise power distribution among the distributed generators (DGs). The droop coefficients in both the DGs have similar values so, both DGs generate the same amount of active power and the reactive power. The output waveform of voltage and current are stable, and its shape is pure sinusoidal. Proposed VMPC along with droop control is used for parallel operation of DGs in islanded for stable operation.

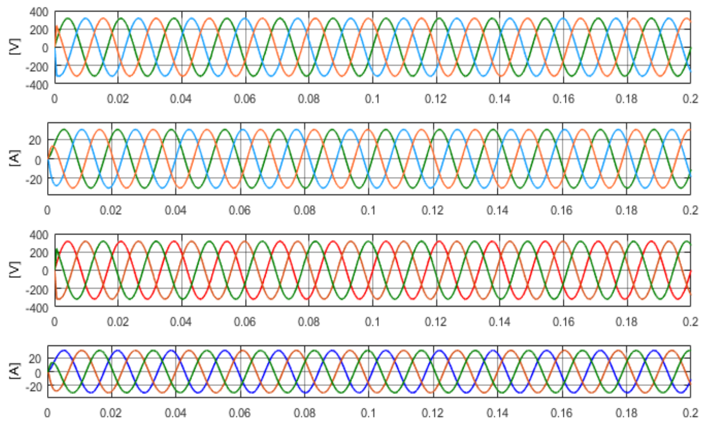

Figure 21. Output voltage and current in islanded mode of both parallel DGs.

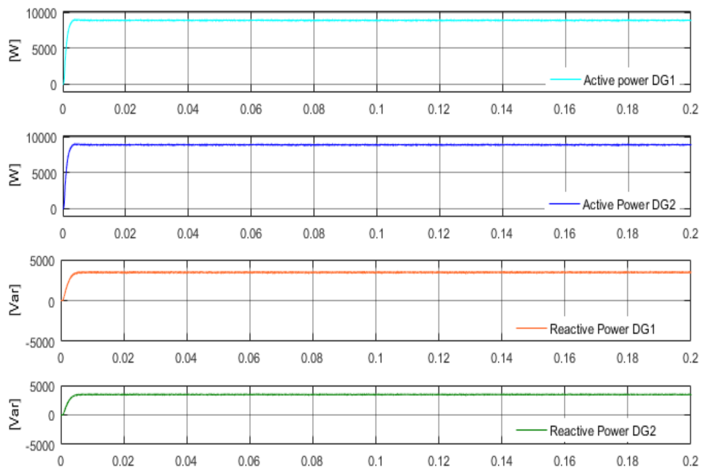

Figure 22. Active and reactive Power of both parallel DGs under linear load in islanded mode of MG

4) Step change of linear load test

This test is performed to show that robustness of VMPC for parallel operation of DGs in islanded. At time t=0.001s total load connected with system is P= 18Kw and Q=7Kvar but at time t=0.1, an additional load is added into system so now P= 28Kw and Q=11Kvar. As the load increases the system generates the power which is also increasing to fulfill the load demand. This waveform shows that the VMPC is robust against the sudden change of load and handles it effectively as shown in Figure 23 and Figure 24 respectively.

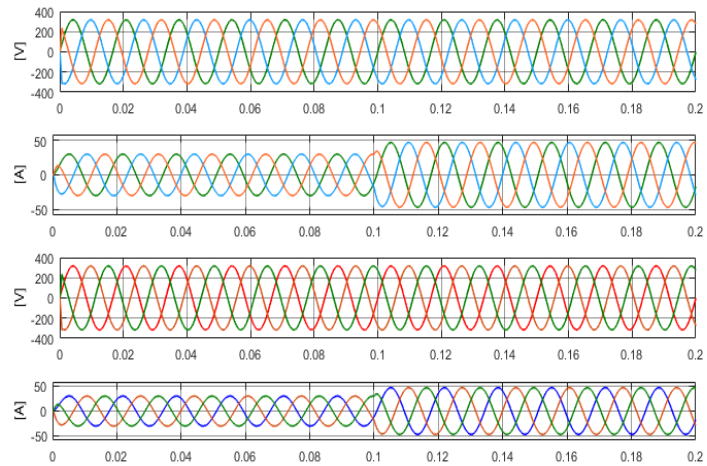

Figure 23. Waveform of output voltage and current of both parallel DGs under linear load transients in islanded mode.

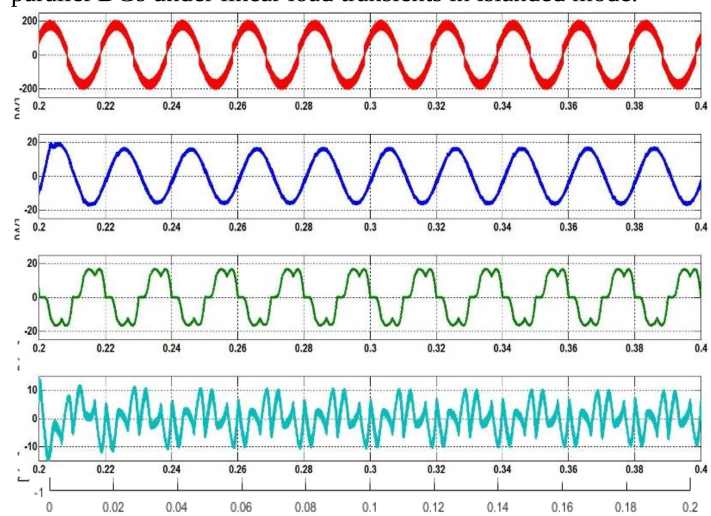

Figure 24: output waveform of active and reactive Power of both parallel DGs under Linear load transients in islanded mode of MG

C. Inverter Operating in Mode 2: Active Power Filtering

During mode 2 of the inverter operation, the active power filtering capability is achieved. The tested simulation results show the system robustness and high APF performance. The simulation waveforms consist of line voltage THDv, utility line current THDi, utility filter current THDi, and DC link voltage. These results prove the system working in terms if harmonic mitigation and filtering with small volumetric size and less cost. All the waveforms are recorded in the MAT-LAB interface. The three-phase nonlinear rectifier load displays the information of THD*i* of 30.1%. The measured THD*i* is above the limitation of grid harmonics according to IEC and IEEE standards. As mentioned earlier, according to the IEEE-519 standard the THD*i* of the grid should be below 5%. The utility voltage, source current, load current, and filter mitigation current simulation waveforms are depicted in Figure 25. The waveforms are detailed in the following sequence: utility voltage v_{Sabc}, utility current i_{Sabc}, load current i_{Labc} filter compensation current i_{Fabc} and DC-link capacitor voltage v_{DC}. The simulation results show that the utility current and load current waveforms are distorted and non-sinusoidal wave shape with high levels of THD*i*. As recorded, after APF operation, the utility current waveform is in sinusoidal wave shape as detailed, the load current wave shape is distorted due to the behavior of the nonlinear load.

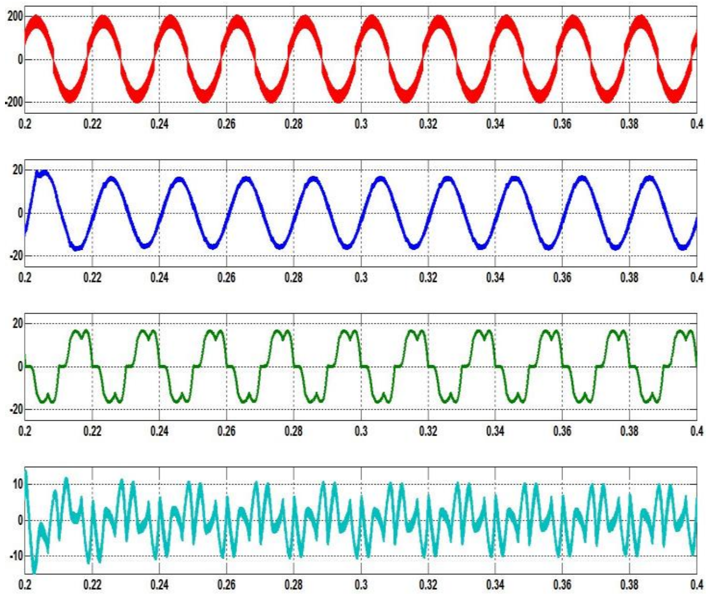

Figure 25. APF operation of system. a) Utility voltage (THD*v*=3.9%) b) Utility current (THD*i*=4.1%) c) Load current (THD*i*=30.1%) d) Counteracting filter current.

The system controlled the DC-link voltage in the range of steady operation of the APF. Therefore, no spare DC power supply is needed. During the countering filter current injection at the PCC, there will be a jump in the DC-link voltage across the DC capacitor of the inverter. This rise of waveform is recorded around 10% and continues constant during the overall operation of mode 2, as depicted in Figure 4.9. The step-change behavior of the DC-link voltage remains for a small period of 0 to 0.05 sec showing no stability issue. In summary, the THD of the utility current and utility voltage is below 5% during critical operational circumstance. The THD is reduced to 4.1% during the APF operation, before the filtering the THD was 30.1%.

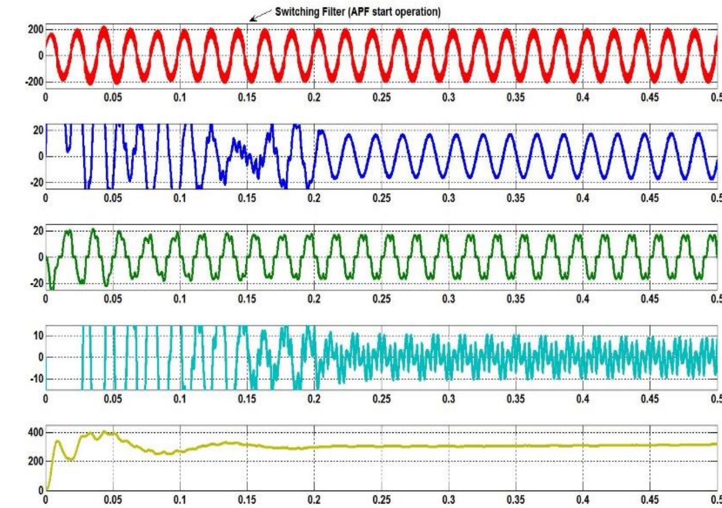

Figure 26. APF operation of system at PCC. a) Utility voltage (THD*v*=3.9%), b) Utility current (THD*i*=4.1%), c) Load current (THD*i*=30.1%), d) Counteracting filter current, e) DC-link capacitor voltage.

Figure 27 proves the starting operation of the APF action. The APF injects the filtering current to neutralize the distorted waveform of the non-linear load. At time interval of 0.12 ms, the APF starts the operation and eliminates the odd harmonics in the current waveform. As noticed, before the APF operation, the utility current and load current waveforms are distorted but after the APF operation, the utility current appears less distorted and stable waveform. Therefore, the THD of the supply current has been reduced to 4.1% effectively from 30.1%. The harmonic spectrum shows the filtering and non-filtering utility current before and after the neutralizing filtering current, as depicted in Figure 28.

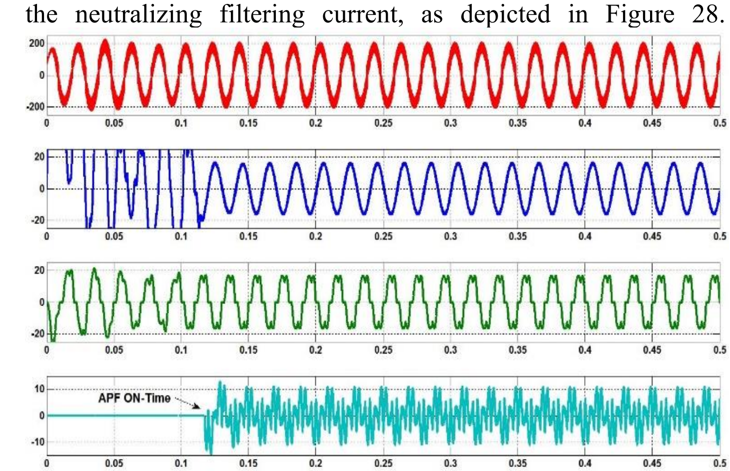

Figure 27. Opening action of APF. a) Utility voltage (THD*v*=3.9%), b) Utility current (THD*i*=4.1%), c) Load current (THD*i*=30.1%), d) Counteracting current at t=0.12 ms.

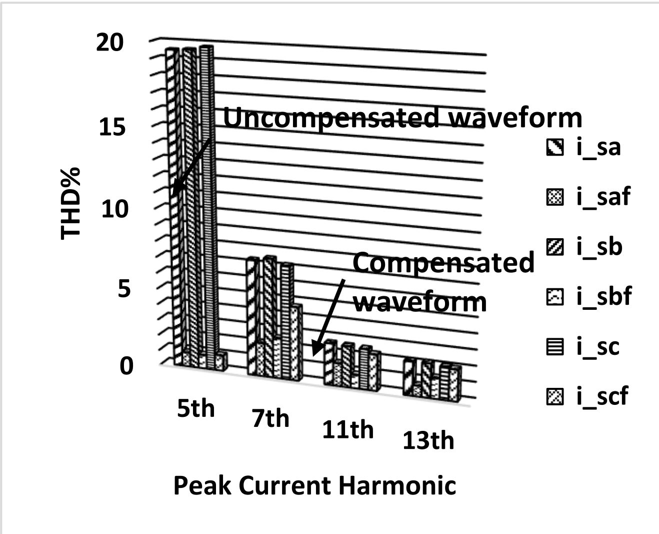

Figure 28. Harmonic spectrum during mode 2 APF operation.

D. High-Current Density Bidirectional DC-DC converter

The proposed bidirectional DC-DC converter operates in dual mode i.e. the charging mode of the battery G2V and the discharging mode of the battery V2G mode of operation. Therefore, the results for both the modes have been presented respectively. Table 4 presents the parameters of the bidirectional DC-DC converter. The constructed circuit serves to validate the feasibility of the battery charger and the battery discharger, functioning within a DC-link voltage range v_{DC} of 600V and a battery voltage v_{Bat} of 200V. The value of the switching frequency is set at 20 kHz, and the high-frequency transformer with turns ratio (N) of 3, features a magnetizing inductance of 107 uH.

1) Battery Discharging Mode:

In the V2G mode during the battery discharging mode, the bidirectional DC-DC converter elevates the lower voltage levels of the battery bank to a regulated high DC-link voltage of 600V. As depicted in Figure 29, the output voltage of the bidirectional DC-DC converter is sustained at 600V, accompanied by an output current of 30A. Figure 30 shows the switch S1, the current waveform and the drain to source voltage in consideration of gate signal. The v_{Ds} of the switches S1 and S2 is under acceptable voltage and current stress.

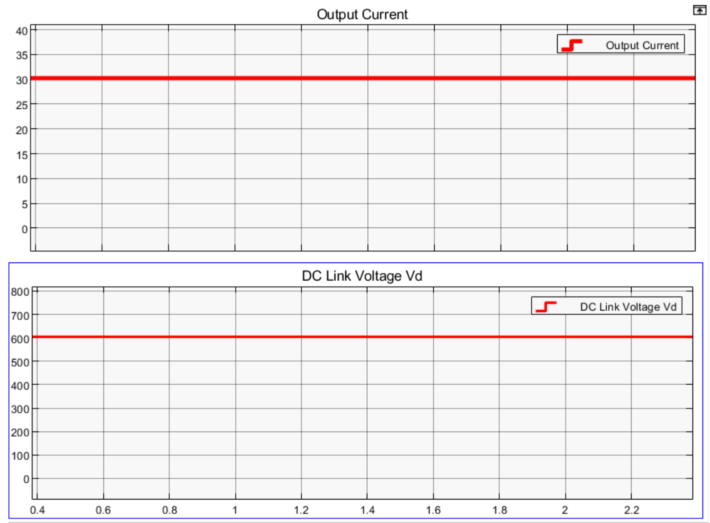

Figure 29. DC-link voltage and current at the output.

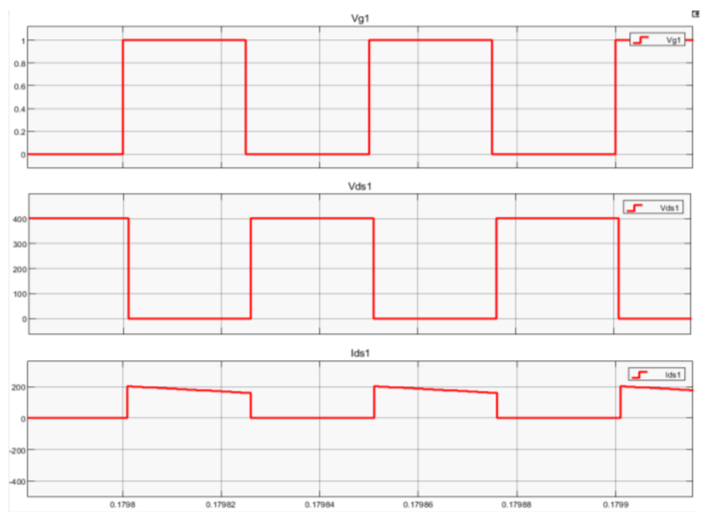

Figure 30. Gate Signal, Drain to Source Voltage V_{DS}, and Drain to Source Current i_{DS}

2) Battery Charging Mode

During Battery Charging mode the DC-link voltage is brought down to low voltage of 200 V_{dc} of the EV battery. The battery bank voltage and the battery bank charging current are shown in Figure 31. The battery current is regulated to 20 A for efficient battery charging. Similarly, the drain to source voltage of the switch as well as the switch current waveform has been shown the smooth operation with low voltage and current stress across switch S3.

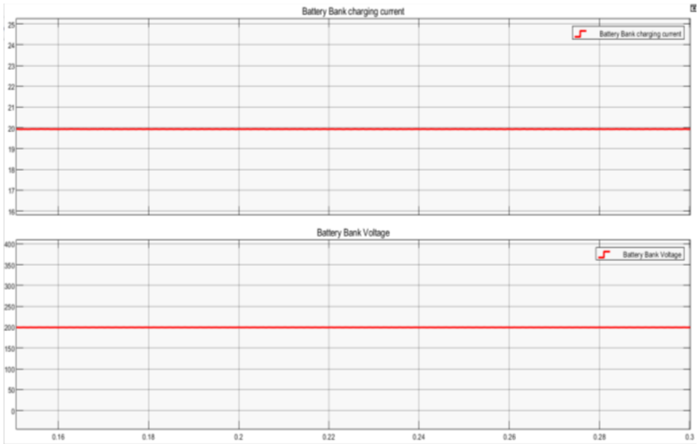

Figure 31. EV Battery Bank Voltage and Battery Charging current.

IV. CONCLUSION

In this paper a new V2G and G2V charging infrastructure has been proposed keeping in view the growing demand of electric vehicles in the market. The infrastructure consists of frontend converter/inverter connected to the grid and the backend novel high current density bidirectional dc-dc converter for EV battery charging and discharging. The whole system is designed to keep the number of switches considerably less than the conventional infrastructure used in the literature. The voltage stress across the switches is under the limits with additional galvanic isolation using high frequency transformer which is important for grid application. This results in reducing the size and weight of the system. Moreover, it improves the efficiency of the system. The system operates in three modes of operation. The model predictive control is proposed of the control of both the high current density bidirectional dc-dc control as well as converter/inverter. The MPC shows exemplary performance for both the converters with regulated dc-link voltage as well as the grid voltage. Besides the inverter also provides better performance for non-linear load as well as transient condition. The active power filter control operating in mode three is responsible for harmonics reduction in the grid. All the results have been validated using intensive simulations.

1.1 REFERENCES

[1] M. A. Nasab, W. K. Al-Shibli, M. Zand, B. Ehsan-maleki, and S. Padmanaban, "Charging management of electric vehicles with the presence of renewable resources," *Renewable Energy Focus,* vol. 48, p. 100536, 2024/03/01/ 2024.

[2] R. K. Lenka, A. K. Panda, and L. Senapati, "Grid integrated multifunctional EV charging infrastructure with improved power quality," *Journal of Energy Storage,* vol. 76, p. 109637, 2024/01/15/ 2024.

[3] M. Zagow, M. Elbany, and A. M. Darwish, "Identifying Urban, Transportation, and Socioeconomic Characteristics Across US Zip Codes Affecting CO2 Emissions: A Decision Tree Analysis," *Energy and Built Environment,* 2024/01/19/ 2024.

[4] N. A. S. Elminshawy, S. Diab, Y. E. S. Yassen, and O. Elbaksawi, "An energy-economic analysis of a hybrid PV/wind/battery energy-driven hydrogen generation system in rural regions of Egypt," *Journal of Energy Storage,* vol. 80, p. 110256, 2024/03/01/ 2024.

[5] R. Karthikeyan and K. Boopathy, "A composite strategy for designing efficient harmonic compensators in grid connected inverters with reduced power," *Measurement: Sensors,* vol. 31, p. 101009, 2024/02/01/ 2024.

[6] W. Al Hanaineh, J. Matas, M. Bakkar, J. El Mariachet, and J. M. Guerrero, "A robust THD based communication-less protection method for electrical grids with DGs," *International Journal of Electrical Power & Energy Systems,* vol. 155, p. 109546, 2024/01/01/ 2024.

[7] S. Umar *et al.*, "A building integrated solar PV surface-cleaning setup to optimize the electricity output of PV modules in a polluted atmosphere," *Renewable Energy,* vol. 216, p. 119122, 2023/11/01/ 2023.

[8] J. Pasha *et al.*, "Electric vehicle scheduling: State of the art, critical challenges, and future research opportunities," *Journal of Industrial Information Integration,* vol. 38, p. 100561, 2024/03/01/ 2024.

[9] S. S. Trivedi and A. V. Sant, "Comparative analysis of dual active bridge dc–dc converter employing Si, SiC and GaN MOSFETs for G2V and V2G operation," *Energy Reports,* vol. 8, pp. 1011-1019, 2022/11/01/ 2022.

[10] I. Ahmed, M. Adnan, M. Ali, and G. Kaddoum, "Supertwisting sliding mode controller for grid-to-vehicle and vehicle-to-grid battery electric vehicle charger," *Journal of Energy Storage,* vol. 70, p. 107914, 2023/10/15/ 2023.

[11] I. Ahmed, H. M. M. Adil, S. Ahmed, I. Ahmad, and Z. Rehman, "Robust nonlinear control of battery electric vehicle charger in grid to vehicle and vehicle to grid applications," *Journal of Energy Storage,* vol. 52, p. 104813, 2022/08/01/ 2022.

[12] S. Adhikary, P. K. Biswas, C. Sain, S. B. Thanikanti, and N. I. Nwulu, "Bidirectional converter based on G2V and V2G operation with time of usage-based tariff analysis and monitoring of charging parameters using IoT," *Energy Reports,* vol. 9, pp. 5404-5419, 2023/12/01/ 2023.

[13] H. Karneddi and D. Ronanki, "Reconfigurable Battery Charger With a Wide Voltage Range for Universal Electric Vehicle Charging Applications," *IEEE Transactions on Power Electronics,* vol. 38, no. 9, pp. 10606-10610, 2023.

[14] N. Sujitha and S. Krithiga, "RES based EV battery charging system: A review," *Renewable and Sustainable Energy Reviews,* vol. 75, pp. 978-988, 2017/08/01/ 2017.

[15] !!! INVALID CITATION !!! (Monteiro, Pinto et al. 2019, Rodrigues, Ferreira et al. 2022).

[16] P. Meenalochini, P. R.A, R. Pugalenthi, and J. A, "Energy management of grid connected PV with efficient inverter based wireless electric vehicle battery charger: A hybrid CSA-QNN technique," *Journal of Energy Storage,* vol. 80, p. 110255, 2024/03/01/ 2024.

[17] M. Grenier, M. G. H. Aghdam, and T. Thiringer, "Design of on-board charger for plug-in hybrid electric vehicle," *IET Conference Proceedings,* pp. 152-152Available: https://digital-library.theiet.org/content/conferences/10.1049/cp.2010.0101

[18] J. Weimer, N. Weimer, J. Nuzzo, and I. Kallfass, "High power density battery chargers with fast-charging utilizing heat storage," *Applied Thermal Engineering,* vol. 232, p. 121043, 2023/09/01/ 2023.

[19] B. Tekgun, D. Tekgun, and I. Alan, "A multi-functional quasi-single stage bi-directional charger topology for electric vehicles," *Ain Shams Engineering Journal,* vol. 15, no. 3, p. 102471, 2024/03/01/ 2024.

[20] S. Jayalath and A. Khan, "Design, challenges, and trends of inductive power transfer couplers for electric vehicles: A review," *IEEE Journal of Emerging and Selected Topics in Power Electronics,* vol. 9, no. 5, pp. 6196-6218, 2020.

[21] G. A. Covic, J. T. Boys, M. L. G. Kissin, and H. G. Lu, "A Three-Phase Inductive Power Transfer System for Roadway-Powered Vehicles," *IEEE Transactions on Industrial Electronics,* vol. 54, no. 6, pp. 3370-3378, 2007.

[22] S. Ketsingsoi and Y. Kumsuwan, "An Off-line Battery Charger based

on Buck-boost Power Factor Correction Converter for Plug-in Electric Vehicles," *Energy Procedia,* vol. 56, pp. 659-666, 2014/01/01/ 2014.

[23] X. Tian, H. Zha, Z. Tian, G. Lang, and L. Li, "Carbon emission reduction capability assessment based on synergistic optimization control of electric vehicle V2G and multiple types power supply," *Energy Reports,* vol. 11, pp. 1191-1198, 2024/06/01/ 2024.

[24] W. Kempton and J. Tomić, "Vehicle-to-grid power implementation: From stabilizing the grid to supporting large-scale renewable energy," *Journal of Power Sources,* vol. 144, no. 1, pp. 280-294, 2005/06/01/ 2005.

[25] S. Singirikonda *et al.*, "Adaptive control-based Isolated bi-directional converter for G2V& V2G charging with integration of the renewable energy source," *Energy Reports,* vol. 8, pp. 11416-11428, 2022/11/01/ 2022.

[26] Y. J. Lee, A. Khaligh, and A. Emadi, "Advanced Integrated Bidirectional AC/DC and DC/DC Converter for Plug-In Hybrid Electric Vehicles," *IEEE Transactions on Vehicular Technology,* vol. 58, no. 8, pp. 3970-3980, 2009.

[27] N. D. Weise, G. Castelino, K. Basu, and N. Mohan, "A Single-Stage Dual-Active-Bridge-Based Soft Switched AC–DC Converter With Open-Loop Power Factor Correction and Other Advanced Features," *IEEE Transactions on Power Electronics,* vol. 29, no. 8, pp. 4007-4016, 2014.

[28] F. Angizeh, J. Bae, J. Chen, A. Klebnikov, and M. A. Jafari, "Impact Assessment Framework for Grid Integration of Energy Storage Systems and Renewable Energy Sources Toward Clean Energy Transition," *IEEE Access,* vol. 11, pp. 134995-135005, 2023.

[29] Y. Luo, B. Zeng, W. Zhang, Y. Liu, Q. Shi, and W. Liu, "Coordinative Planning of Public Transport Electrification, RESs and Energy Networks for Decarbonization of Urban Multi-Energy Systems: A Government-Market Dual-Driven Framework," *IEEE Transactions on Sustainable Energy,* vol. 15, no. 1, pp. 538-555, 2024.

[30] T. Mai *et al.*, "Renewable Electricity Futures for the United States," *IEEE Transactions on Sustainable Energy,* vol. 5, no. 2, pp. 372-378, 2014.

[31] S. Ganesan, U. Subramaniam, A. A. Ghodke, R. M. Elavarasan, K. Raju, and M. S. Bhaskar, "Investigation on Sizing of Voltage Source for a Battery Energy Storage System in Microgrid With Renewable Energy Sources," *IEEE Access,* vol. 8, pp. 188861-188874, 2020.

[32] S.-K. Hong, S. G. Lee, and M. Kim, "Assessment and Mitigation of Electric Vehicle Charging Demand Impact to Transformer Aging for an Apartment Complex," *Energies,* vol. 13, no. 10, p. 2571, 2020.

[33] J.-M. Clairand, C. Álvarez-Bel, J. Rodríguez-García, and G. Escrivá-Escrivá, "Impact of Electric Vehicle Charging Strategy on the Long-Term Planning of an Isolated Microgrid," *Energies,* vol. 13, no. 13, p. 3455, 2020.

[34] B. E. Lebrouhi, Y. Khattari, B. Lamrani, M. Maaroufi, Y. Zeraouli, and T. Kousksou, "Key challenges for a large-scale development of battery electric vehicles: A comprehensive review," *Journal of Energy Storage,* vol. 44, p. 103273, 2021/12/15/ 2021.

[35] R. C. Green, L. Wang, and M. Alam, "The impact of plug-in hybrid electric vehicles on distribution networks: A review and outlook," *Renewable and Sustainable Energy Reviews,* vol. 15, no. 1, pp. 544-553, 2011/01/01/ 2011.

[36] Y. L. Lou, C. X. Wu, Z. Z. Shi, and R. Yang, "Evaluation of EV penetration level limit in distribution system applying charging and scheduling strategies," *Sustainable Energy, Grids and Networks,* vol. 32, p. 100922, 2022/12/01/ 2022.

[37] M. Secchi, G. Barchi, D. Macii, and D. Petri, "Smart electric vehicles charging with centralised vehicle-to-grid capability for net-load variance minimisation under increasing EV and PV penetration levels," *Sustainable Energy, Grids and Networks,* vol. 35, p. 101120, 2023/09/01/ 2023.

[38] M. Kesler, M. C. Kisacikoglu, and L. M. Tolbert, "Vehicle-to-Grid Reactive Power Operation Using Plug-In Electric Vehicle Bidirectional Offboard Charger," *IEEE Transactions on Industrial Electronics,* vol. 61, no. 12, pp. 6778-6784, 2014.

[39] V. Monteiro, J. C. Ferreira, A. A. N. Meléndez, C. Couto, and J. L. Afonso, "Experimental Validation of a Novel Architecture Based on a Dual-Stage Converter for Off-Board Fast Battery Chargers of Electric Vehicles," *IEEE Transactions on Vehicular Technology,* vol. 67, no. 2, pp. 1000-1011, 2018.

[40] H. J. Chiu, Y. K. Lo, C. J. Yao, T. P. Lee, J. M. Wang, and J. X. Lee, "A Modular Self-Controlled Photovoltaic Charger With InterIntegrated Circuit ($\hbox{I}^{2}\hbox{C}$) Interface," *IEEE Transactions on Energy Conversion,* vol. 26, no. 1, pp. 281-289, 2011.

[41] D. Razmi, T. Lu, B. Papari, E. Akbari, G. Fathi, and M. Ghadamyari, "An Overview on Power Quality Issues and Control Strategies for Distribution Networks With the Presence of Distributed Generation Resources," *IEEE Access,* vol. 11, pp. 10308-10325, 2023.

[42] C. Gong, Z. Cheng, W. K. Sou, C. S. Lam, and M. Y. Chow, "Collaborative Distributed Optimal Control of Pure and Hybrid Active Power Filters in Active Distribution Network," *IEEE Transactions on Power Delivery,* vol. 38, no. 4, pp. 2326-2337, 2023.

[43] H. Lee and J. Shon, "Non-Integral AC Capacitor Voltage Calculation Method for Shunt Hybrid Active Power Filter," *IEEE Access,* vol. 11, pp. 67968-67978, 2023.

[44] Y. T. Wassie and E. O. Ahlgren, "Understanding the load profiles and electricity consumption patterns of PV mini-grid customers in rural off-grid east africa: A data-driven study," *Energy Policy,* vol. 185, p. 113969, 2024/02/01/ 2024.

[45] S. Das, H. M. Ishrak, M. M. Hasan, and M. A. Kabir, "Empirical analysis of power quality using UPQC with hybrid control techniques," *Results in Engineering,* vol. 20, p. 101527, 2023/12/01/ 2023.

[46] K. M. Nagabushanam *et al.*, "Development of high-gain switched-capacitor based bi-directional converter for electric vehicle applications," *Journal of Energy Storage,* vol. 82, p. 110602, 2024/03/30/ 2024.

[47] D. E. Quevedo, R. P. Aguilera, M. A. Perez, P. Cortes, and R. Lizana, "Model predictive control of an AFE rectifier with dynamic references," *IEEE transactions on power electronics,* vol. 27, no. 7, pp. 3128-3136, 2011.

[48] A. Jabbarnejad, S. Vaez-Zadeh, M. Khalilzadeh, and M. Eslahi, "Model-Free Predictive Control for Grid-Connected Converters with Flexibility in Power Regulation: a Solution for Unbalanced Conditions," *IEEE Journal of Emerging and Selected Topics in Power Electronics,* 2024.

[49] S. Vazquez *et al.*, "Comparison between FS-MPC control strategy for an UPS inverter application in α-β and abc frames," in *2010 IEEE International Symposium on Industrial Electronics*, 2010, pp. 3133-3138: IEEE.

[50] T. Oliveira, L. Caseiro, A. Mendes, and S. Cruz, "Finite control set model predictive control for paralleled uninterruptible power supplies," *Energies,* vol. 13, no. 13, p. 3453, 2020.

[51] H. S. Khan, M. Aamir, M. Ali, A. Waqar, S. U. Ali, and J. Imtiaz, "Finite control set model predictive control for parallel connected online ups system under unbalanced and nonlinear loads," *Energies,* vol. 12, no. 4, p. 581, 2019.

[52] J. Hu, J. Zhu, and D. G. Dorrell, "Model predictive control of grid-connected inverters for PV systems with flexible power regulation and switching frequency reduction," *IEEE Transactions on Industry Applications,* vol. 51, no. 1, pp. 587-594, 2014.

[53] W. U. K. Tareen and S. Mekhielf, "Three-phase transformerless shunt active power filter with reduced switch count for harmonic compensation in grid-connected applications," *IEEE Transactions on Power Electronics,* vol. 33, no. 6, pp. 4868-4881, 2017.

[54] R. Inzunza and H. Akagi, "A 6.6-kV transformerless shunt hybrid active filter for installation on a power distribution system," *IEEE Transactions on power electronics,* vol. 20, no. 4, pp. 893-900, 2005.

[55] X. Zheng, Z. Gong, Z. Liu, Z. Li, D. Yuan, and T. Jin, "Research on Start-stop standby energy storage element participating in wind power filtering under the influence of power quality disturbance," *International Journal of Electrical Power & Energy Systems,* vol. 145, p. 108631, 2023.

1.2 AUTHORS

First Author Tayyaba Gul Tareen, MSc, Iqra National University.

Tayyaba Gul Tareen has received her B.Sc. degree in electrical engineering from the University of Engineering and Technology, Peshawar, Pakistan, in 2007, and the master's degree from CECOS University, Peshawar, Pakistan, in 2011. At present she is working as a Ph.D. scholar in the Power Electronics, Department of Electrical Engineering, Iqra National University, Peshawar, Pakistan. Her research focuses on the Power Quality issues, power conversion methods and electric vehicles.

Second Author – Muhammad Aamir, Department of Electrical and Computer Engineering, Pak Austria Fachhochschule, Institute of Applied Science and Technology, Haripur, Pakistan;

Third Author – Jehanzeb Khana, Department of Electrical Engineering, IQRA National University, Peshawar 25100, Pakistan;

Fourth Author – Ghassan Husnain, Department of Computer Science, CECOS University of IT & Emerging Sciences, Peshawar, Pakistan.

Fifth Author – Fakhar Anjam Department of Electrical Engineering, University of Science & Technology Bannu, Pakistan

Correspondence Author – Tayyaba Gul Tareen,